Proceedings of the ASME 2024 19th International Manufacturing Science and Engineering Conference
MSEC2024
June 17-21, 2024, Knoxville, Tennessee

MSEC2024-125230

PREDICTING MICROSTRUCTURE EVOLUTION IN LASER POWDER BED FUSION ADDITIVE MANUFACTURING USING PHYSICS-BASED MACHINE LEARNING

Alexander Riensche
Virginia Tech
Blacksburg, VA

Benjamin Bevans
Virginia Tech
Blacksburg, VA

Grant King
University of Nebraska
Lincoln, NE

Ajay Krishnan
Edison Welding Institute
Columbus, OH

Kevin Cole
University of Nebraska
Lincoln, NE

Prahalada Rao
Virginia Tech
Blacksburg, VA

ABSTRACT

The long-term goal of this work is to predict and control microstructure evolution in metal additive manufacturing processes. As a step towards this goal, the objective of this paper is the rapid prediction of the microstructure evolution in parts made using the laser powder bed fusion (LPBF) additive manufacturing process. To realize this objective, we developed and applied an approach which combines physics-based thermal modeling with data-driven machine learning to predict two important microstructure-related characteristics in Nickel Alloy 718 LPBF-processed parts: meltpool depth and primary dendritic arm spacing (PDAS). Microstructure characteristics are critical determinants of functional physical properties, e.g., yield strength and fatigue life. Currently, the microstructure of laser powder bed fusion parts is optimized through a cumbersome and costly build-and-characterize empirical approach. This makes the development of rapid and accurate models for predicting microstructure evolution practically valuable: these models reduce process development time and enable fabrication of parts with consistent properties. Unfortunately, due to their computational complexity, existing physics-based models for predicting microstructure evolution are limited to only a few layers and are challenging to scale to practical parts. To overcome the drawbacks of current microstructure prediction techniques, this paper establishes a novel physics and data integrated modeling approach. The approach consists of two steps. First, a rapid, part-level computational thermal model was used to predict the temperature distribution and cooling rate in the entire part before it was printed. Second, the foregoing physics-based thermal history quantifiers were used as inputs to a simple machine learning model (support vector machine) trained to predict the meltpool depth and primary dendritic arm spacing based on empirical materials characterization data. As an example of its efficacy, when tested on a separate set of samples from a different build, the approach predicted the PDAS with root mean squared error ≈ 110 nm. The modeling approach was further able to predict meltpool depth with a root mean squared error of 0.012mm. This model performance was validated through the creation of 21 geometries created under 7 different process parameters. Optical and scanning electron microscopy was conducted resulting in more than 1200 primary dendritic arm spacing and meltpool depth measurements. Primary dendritic arm spacing predictions were also validated on parts of a unique geometry created in a separate work. The model was able to successfully transfer to this build without further training, indicating that this method is transferrable to other parts made with laser powder bed fusion and Nickel Alloy 718. This work thus presents an avenue for future physics-based optimization and control of microstructural evolution in laser powder bed fusion.

Keywords: Microstructure Evolution, Meltpool Depth, Thermal Modeling, Physics-based Machine Learning

1. INTRODUCTION

Laser powder bed fusion (LPBF) is an additive manufacturing process that enables creation of advanced geometries that are impossible to produce through traditional manufacturing methods. Furthermore, the process has been shown to significantly reduce part lead times, particularly where complexity drives up production cycle times [1, 2]. Despite these benefits, the process has not seen widespread adoption in industry. One key reason for the reticent adoption in industry is the tendency of the process tendency to generate heterogeneous microstructures, which in turn produces parts with inconsistent mechanical properties [3, 4].

The goal of this work is to predict microstructure evolution in parts created using the LPBF additive manufacturing process. To achieve this goal, we developed and applied an approach that

combines physics-based thermal modeling with data-driven machine learning. Rapid, accurate prediction of microstructure has the potential to reduce the cost of additive manufacturing as well as expand its applications by reducing qualification time of parts and enabling the creation of consistent functional properties such as yield strength, creep and fatigue life [5, 6].

Microstructure evolution in LPBF is controlled by a variety of parameters including laser power, laser velocity, and part shape. Current methods to qualify and obtain desired part properties use an empirical build-and-test approach with a specific material and geometry. Sample coupons are tested using non-destructive and destructive techniques to verify microstructure, but unfortunately these methods do not scale well to larger geometries. Furthermore, qualification must be completed on a per-geometry basis, as any change in the part may significantly affect the microstructure obtained.

The objective of this work is to predict the microstructure obtained in LPBF by correlating model-derived temperature fields (otherwise known as thermal history) with specific microstructure characteristics. In this work, two microstructure properties are predicted: meltpool depth and primary dendritic arm spacing (PDAS) as a function of sub-surface (100 µm from the top surface) thermal phenomena. This framework is summarized in FIGURE 1. This process is unique as it requires no sensor data or computationally expensive thermomechanical and microstructure modeling techniques, making this method highly relevant for effective industrial application.

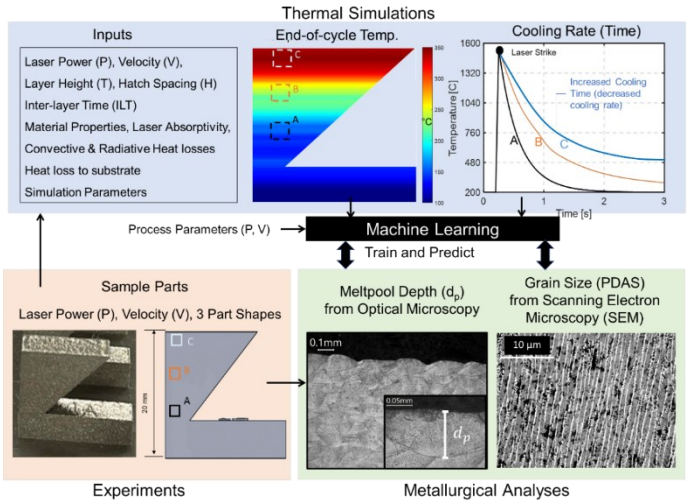

FIGURE 1: A SUMMARY OF THE APPROACH OF THIS WORK FOR THE PREDICTION OF MELTPOOL DEPTH AND PRIMARY DENDRITIC ARM SPACING (PDAS). THERMAL MODEL-DERIVED FEATURES ARE COMBINED WITH DATA-DRIVE MACHINE LEARNING IN ORDER TO PREDICT MICROSTRUCTURE FEATURES IN A RAPID, INDUSTRIALLY RELEVANT MANNER.

2. MATERIALS AND METHODS

2.1 Experimental Setup

Parts were created for this experiment in partnership with Edison Welding Institute using their open architecture LPBF system. A long-wave infrared camera (Micro-Epsilon TIM 640) is installed in the build chamber, placed with a view 80° to the horizontal. This was used to validate thermal history predictions in this work. The system layout and sensor arrangement can be seen in FIGURE 2. The camera recorded the thermal trends for the top surface of all parts created in the build. The camera was calibrated to measure the temperatures in the range of 25°C to 250°C using a black-body technique used in our previous works [7, 8].

The geometries printed include 21 samples of a simple overhang, as well as four cubes used to calibrate the installed infrared camera. The material chosen for this work was Nickel Alloy 718 (Inconel 718) due to its importance in the defense and aerospace industries [9, 10]. The material was also selected based on our previous experience working with it, which provided understanding of the effects of process parameters on porosity and part deformation. These defects confound microstructure formation, so it is imperative to use parameters which do not induce these flaws [7, 8].

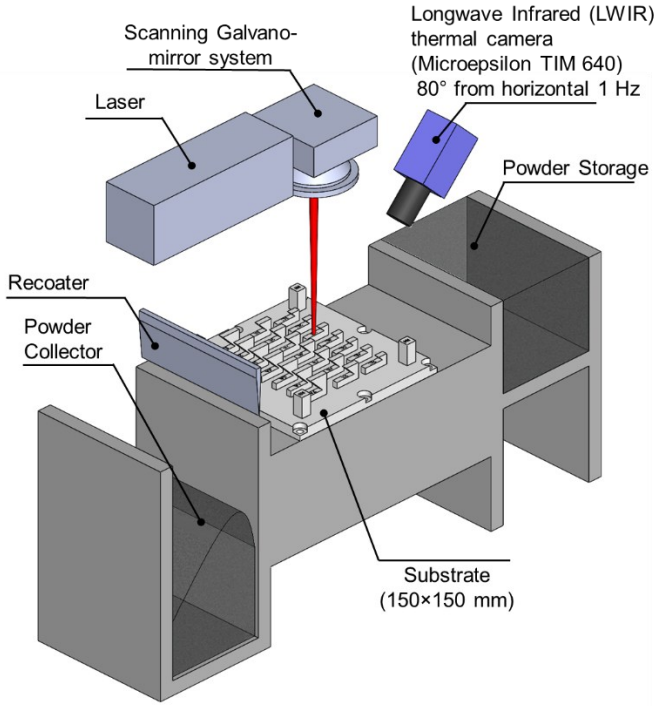

FIGURE 2: SCHEMATIC OF THE OPEN ARCHITECTURE LPBF SYSTEM. AN INFRARED CAMERA WAS PLACED 80° FROM THE HORIZONTAL TO MEASURE SURFACE TEMPERATURE.

The overhang sample was divided into three build heights. These parts are denoted as A-type, B-type, and C-type, with build heights of 10mm, 15mm, and 20mm respectively. The total build time was approximately six hours. Seven process parameter

combinations were tested. Parameter combinations were created by changing laser power and scan speed in steps of ±30% increments from the manufacturer-recommended settings of 285W laser power and 960 mm·s^{-1} scan speed. The design of the build plate, as well as the details of all samples and parameter combinations tested in this work are shown in FIGURE 3. Other processing conditions, such as layer thickness and hatch spacing were maintained as constant.

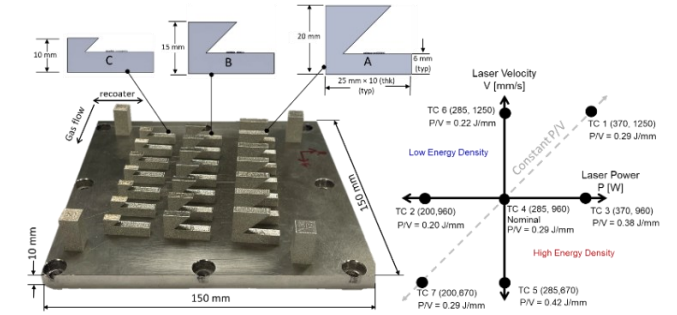

FIGURE 3: (LEFT) THE FINISHED BUILD WITH A SCHEMATIC OF THE THREE DIFFERENT OVERHANG PARTS CREATED IN THIS WORK. ALL DIMENSIONS ARE IN MM. (RIGHT) THE SELECTED PROCESS PARAMETERS USED IN THIS WORK

2.2 Materials Characterization

Each of the 21 samples was examined with a Nikon 225XTH X-ray computed tomography (XCT) system with a voxel resolution of 16 µm. All samples tested showed negligible porosity with defect volume ratio (DVR) less than 0.01% for all samples tested. By avoiding porosity formation, unintended variation in microstructure is avoided which would confound the microstructure formation factors.

After XCT was completed, the parts were cut in half along the XZ plane to quantify the meltpool penetration depth and primary dendritic arm spacing (PDAS). Meltpool depth measurements were conducted according to NASA MSFC-SPEC-3717, which is visually shown in FIGURE 4 [11, 12]. Parts were cross-sectioned, polished and etched in order to expose the resulting meltpool penetrations. Meltpool depth was quantified by measuring the distance from the top surface of the part to the furthest point on the corresponding meltpool hatch (d_p). The ratio of the measured depth to the nominal layer thickness $\left(\frac{d_p}{L}\right)$ is also used as a metric. This metric is used as a guide of optimal meltpool penetration, as practitioners at Edison Welding Institute stated that $\frac{d_p}{L}$ ratio greater than 2 is preferred. In this work, 1250 measurements were obtained across all 21 samples.

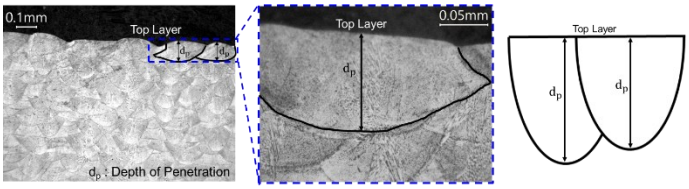

FIGURE 4: METHOD FOR MEASURING MELTPOOL DEPTH PER NASA MSFC-SPEC-3717 **[12]**. THE SPECIFICATION LIMITES MELTPOOL DEPTH MEASUREMENT TO THE TOP-MOST LAYER IN ORDER TO HAVE A DEFINED REFERENCE DATUM.

Grain morphology has a prominent effect on mechanical properties such as creep, strength and microhardness [13, 14]. The polished and etched samples were examined with scanning electron microscopy (SEM) at 6,500x magnification. Each part was sampled in the same regions, demarcated in FIGURE 5. 65 locations were sampled for A-type samples, with 39 and 23 samples taken for each B and C-type sample respectively. All available regions were measured for all samples, resulting in the reduction of measurements for the B and C-type samples. Locations were referenced from the top surface of the part. At each sample location, two images were taken and used to extract PDAS. In total, 1,364 SEM images were acquired across all samples.

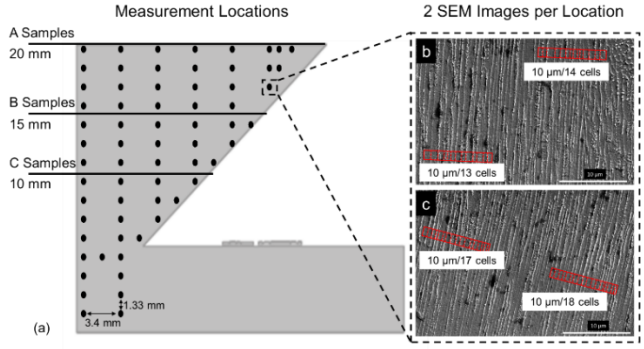

FIGURE 5: (a) LOCATIONS ON THE SAMPLES WHERE SEM IMAGES WERE TAKEN TO MEASURE PDAS. 1364 IMAGES WERE AQUIRED ACROSS ALL 21 SAMPLES. (b,c) SCHEMATIC OF METHOD USED TO MEASURE PDAS FROM SEM IMAGES.

In order to acquire PDAS (λ_1) measurements, two non-overlapping 10 µm regions are drawn perpendicular to the grain growth. Each dendrite that passes through the bounding box is counted and the average dendritic arm spacing is calculated as 10µm divided by the average number of dendrites in the box. This technique can be seen in FIGURE 5. This work focused on variation in microstructure across layers, so the resulting measurements were then averaged across the build direction, resulting in 135 λ_1 measurements.

2.3 Thermal Modeling Approach

Part shape, material properties, machine conditions, and processing parameters all influence microstructure properties such as meltpool depth and PDAS [15]. These factors influence material cooling rates, which in turn drive the final microstructure evolution. To predict temperature distributions on the part-scale in LPBF, the heat diffusion equation must be solved, which is shown in Eq. (1) [16]. The heat diffusion equation provides the temperature T at location (x,y,z) at time instant t.

$$\rho c_p \frac{\partial T(x,y,z,t)}{\partial t} - k\overbrace{\left(\frac{\partial^2}{\partial x^2}+\frac{\partial^2}{\partial y^2}+\frac{\partial^2}{\partial z^2}\right)}^{Laplacian\ operator} T(x,y,z,t) = Q \qquad (1)$$

To use this equation, the second derivative, otherwise called the Laplacian Operator, must be solved. In traditional practice, this equation is solved with the finite element technique. This method, however, is computationally expensive due to the need to remesh the part due to changing geometry in LPBF [17]. This additional computational overhead limits practical application in industry due to it requiring less time to conduct empirical build-and-test optimization compared with simulation techniques.

This work overcomes the limitations of traditional finite element analysis by using a novel, mesh-free graph theory thermal modeling approach to predict part-level thermal history. The method has been shown in previous works to have accuracy comparable to FE simulation methods but solves the thermal history of LPBF geometries approximately 5 times faster [7, 8, 18, 19]. The graph theory method replaces the continuous form of the Laplacian matrix with the discrete Laplacian matrix (L), resulting in the following semi-analytical solution shown in Eq 2.

$$T(x,y,z,t) = \phi e^{-\frac{k}{\rho c_p}\Lambda t}\phi'\left(\frac{A_e S_l}{\rho v c_p}\frac{P}{V} + T_{prev}\right) \quad (2)$$

In this form, the heat diffusion equation is solved as a function of the eigenvalues (Λ) and eigenvectors (ϕ) of the Laplacian Matrix (L), with discrete points chosen to represent the part geometry. A_e is the effective laser absorptivity, S_l length scanned per layer (a function of hatch spacing, [mm]), P [W] laser power, V [mm·s^{-1}] laser velocity, v [mm^3] volume of material melted in a layer (a product of scanned area and layer height), and T_{prev} [°C] is the temperature of the previous layer (from simulation). In this work, Ae = 0.60 based on experiments by Ye et al. at Lawrence Livermore National Laboratory [20].

The method for deriving and implementing the graph theory thermal solution is detailed in our previous works [18]. The graph theory approach has been shown to have similar precision of FE methods while being 2.5 to 5 times faster than commercial finite element solutions [21]. This modeling approach can achieve faster simulation times due to its elimination of the meshing step commonly seen in finite element-based solutions. In this work, the models for A-type parts completed in 3 minutes, with B and C-type parts requiring 2.5 and 2 minutes respectively.

2.4 Machine Learning Approach

To predict microstructure properties, two parameters are extracted using the graph-theory thermal modeling approach which were used as inputs to simple machine learning models, these being cooling time and end-of-cycle temperature. End-of-cycle temperature is extracted as per previous works and can be seen in FIGURE 6(a) [19]. A 1.5mm x 1.5mm area is selected in the base of sample parts, where all thermal history information is extracted. The end-of-cycle temperature quantifies the steady state temperature achieved before the subsequent laser strike. This identifies the overall heat accumulation present in the current part.

The cooling time (t_c), as shown in FIGURE 6(b), is the duration required for the temperature to decrease to 700 °C following the laser strike, approximately half the melting point of Nickel Alloy 718, which has a wide liquidous range from 1260 – 1330 °C [9, 10]. These metrics were acquired 100 µm (2.5 layers) from the topmost layer. Because meltpool penetrations have been observed to be more than one nominal layer thickness, cooling rate information must be extracted below the top layer, which determines the microstructure properties at this point.

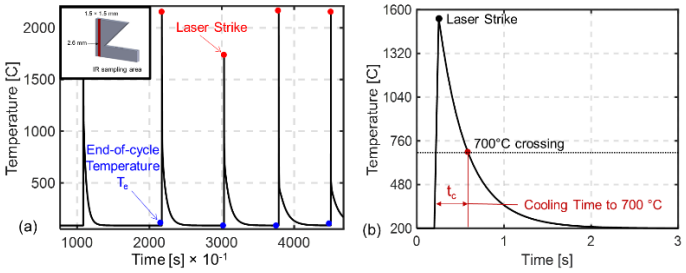

FIGURE 6: (a) THERMAL HISTORY EXTRACTED FROM THE GRAPH THEORY THERMAL MODEL OVER A 1.5X1.5MM AREA. END-OF-CYCLE TEMPERATURE IS EXTRACTED IMMEDEATLY BEFORE THE SUBSEQUENT LAYER. (b) THE COOLLING TIME IS THE DURATION FOR THE TEMPERATURE IN THE SAMPLE AREA TO REDUCE TO 700 °C, OR APPROXIMATLY HALF THE OF THE MELTING POINT IN NICKEL ALLOY 718.

To predict microstructure evolution, elementary machine learning was used. The overall machine learning approach is summarized in FIGURE 7. The cooling time (t_c) and end-of-cycle temperature (T_e) derived from the graph theory thermal simulations, along with the laser power to scan velocity ratio (P/V) serve as inputs to machine learning models. The ground truth microstructure, PDAS and meltpool depth, data for the model are obtained from the materials characterization data obtained in Sec. 2.2.

The machine learning aspect of this work was subdivided into two tasks. Task 1 looks to predict meltpool penetration depth and Task 2 aims to predict the primary dendritic arm spacing of the parts. Each of the tasks are further subdivided into three subtasks which involve classification and regression prediction.

Task 1A and Task 1B classify the meltpool depth into discrete two and three levels, respectively, while Task 1C involves predicting the meltpool depth with regression analysis. Tasks 1A and B employ logistic regression and Gaussian support vector machine (SVM) algorithms. Task 1C analysis uses linear regression and Gaussian SVM regression. While the prediction results could be significantly improved by using complex machine learning models, such as multi-layer artificial neural networks, the tradeoff would be in interpretability and increased uncertainty due to overfitting.

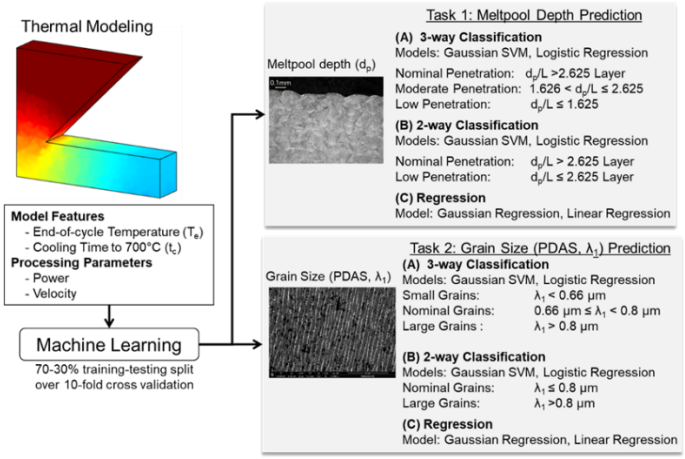

FIGURE 7: THE OVERVIEW OF MACHINE LEARING APPROACH. THE AIM IS TO PREDICT MELTPOOL DEPTH (TASK 1) AND PDAS (TASK 2) AS A FUNCTION OF COOLING TIME AND END-OF-CYCLE TEMPERATURE.

For all tasks, the materials characterization data is split into 70-30% testing-training subsets, and 10-fold cross validation procedure is implemented. For A and B tasks, the results are reported in terms of the F-score, which includes an estimate of both Type 1 and Type 2 errors [22-24] Classes for A and B tasks were derived from feedback from Edison Welding Institute to easily define microstructure performance. For C tasks, the results are quantified in terms of the root mean squared error (RMSE).

Since the relatively smaller number of λ_1 measurements may result in overfitting, a separate validation build was used for testing model transferability and uncertainty quantification. These λ_1 measurements were subsequently used to validate the trained model; the model is not retrained with these new measurements.

3. RESULTS AND DISCUSSION

3.1 Meltpool Depth

The resulting meltpool depths which were obtained using the procedure described in Sec. 2.2 are shown in FIGURE 8 as a function of increasing P/V ratio.

At low energy conditions, the average meltpool depth ranged from 75 to 85 µm. At the nominal condition, the meltpool depth increased to ~110 µm. at equal P/V ratio, the depth varied drastically from 75 to 110 µm with no clear trend observed in the data. These differences in meltpool depth are consistent with observations of Keshavarzkermani *et al.* [25], which demonstrated that meltpool depth can vary independent of process parameter selection. Meltpool depth changed as a function P/V ratio and the layer thickness. Changing process parameters did not consistently predict the final meltpool depth.

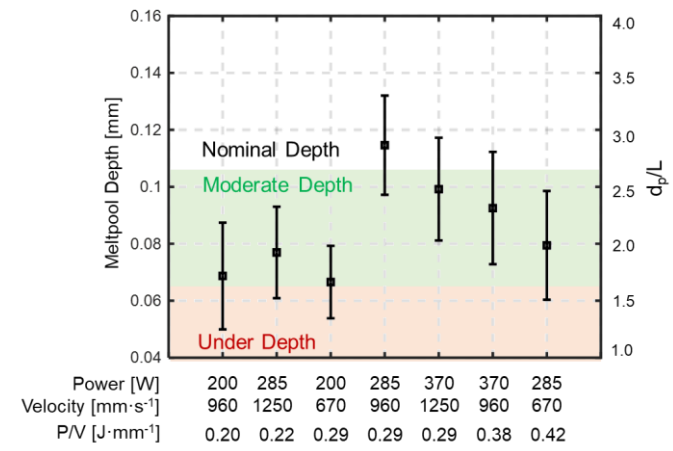

FIGURE 8: MELTPOOL DEPTH AS A FUNCTION OF THE P/V RATIO FROM ALL 21 SAMPLES. THE ERROR BARS ARE FOR ±1σ DEVIATION.

The results reported in FIGURE 8 imply that process parameters have a complex relationship with meltpool depth, which reflects the results of Keshavarzkermani *et al.* [25]; an increase in energy density does not clearly correlate to increased meltpool depth. Increasing P/V ratio can cause meltpool widening, impacting meltpool depth. Moreover, the meltpool standard deviation within the same sample is as large as 20 µm—such large variation results from stochasticity in the process which has been observed in literature [26, 27].

The results of applying machine learning to prediction of meltpool depth are reported in TABLE 1in terms of mean F-score and RMSE from 10-fold training with standard deviation in the parenthesis. For Task 1A and Task 1B the F-score for the 3-way case using the Gaussian SVM model is ~71%, which improved to 83% for the 2-way case. The corresponding logistic regression results are 56% and 67% for the 2-way and 3-way classification, respectively. The results from the logistic regression are inferior because it cannot capture nonlinear data trends observed in this case.

TABLE 1: MACHINE LEARNING RESULTS FOR MELTPOOL DEPTH MODELS

Task 1 Classification F-score (Std.dev)	Task 1A 3-way meltpool depth classification	Logistic Regression: 56% (3%) **Gaussian SVM: 71% (2%)**
	Task 1B 2-way meltpool depth classification	Logistic Regression: 67% (5%) **Gaussian SVM: 83% (3%)**
Task 2 Regression (RMSE)	Task 1C Meltpool depth prediction	Linear Regression: $d_p = 0.021$ mm ($d_p/L = 0.52$) **Gaussian SVM Regression $d_p = 0.012$ mm ($d_p/L = 0.3$)**

The prediction error was improved through the use of SVM regression, which resulted in a root mean square error of ~ 12 µm, or 1/3 of a layer The error increases to 1/2 layer with the simple linear regression model. The prediction error is a result of stochastic process variation, which is caused by local variations in the meltpool commonly observed in literature with in-situ meltpool optical and pyrometry imaging [24].

3.2 Primary Dendritic Arm Spacing

The resulting PDAS measurements as acquired per Sec. 2.2 are shown in FIGURE 9. From these results, it is obvious from these results that PDAS increases with increasing energy density; λ_1 increases from 0.67 µm for TC 2 (P/V = 0.20 J·m^{-1}) to nearly 1 µm for TC 5 (P/V = 0.42 J·m^{-1}). This analysis indicates that process parameters are an insufficient predictor of primary dendritic arm spacing.

Despite the P/V ratio being the same for TC 7, 4, and 1 which resulted in the same effective energy density, there is a prominent difference in λ_1. This relationship is expected to further break down with more complex geometry. This analysis further does not consider variation in λ_1 due to changing part geometry and is unable to capture changing λ_1 due to change in build height. Process modeling and prediction allows for prediction of all build heights, allowing variation in microstructure to be predicted.

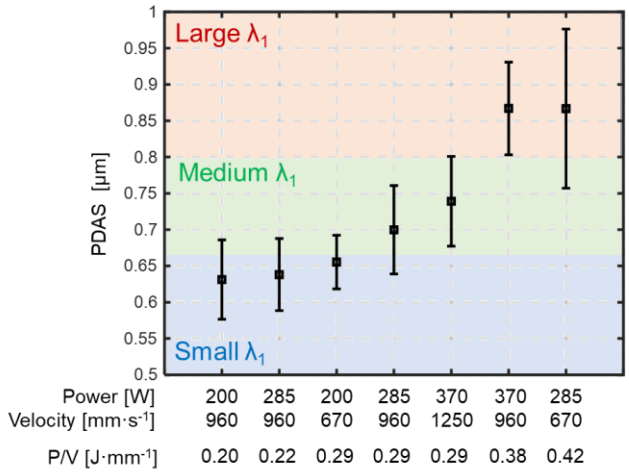

FIGURE 9: THE MEAN PRIMARY DENDRITIC ARM SPACING (PDAS) AS A FUNCTION OF THE PROCESSING PARAMETERS ARRANGED IN ORDER OF P/V RATIO. THE ERROR BARS ARE FOR ±1σ DEVIATION. PDAS TENDS TO INCREASE DUE TO HEAT BUILDUP, HOWEVER THERE IS SIGNIFICANT VARAITION IN PDAS, ESPECIALLY FOR TREATMENT CONDITIONS WHERE P/V RATIO IS IDENTICAL.

FIGURE 10 shows the graph theory predicted end-of-cycle temperature and cooling time as a function of build height on the largest A-type samples. (λ_1) measurements in their respective measurement locations on the A-type samples are shown in the same figure for four of the samples. The higher end-of-cycle temperature (T_e) and cooling time (t_c) are represented with red hue spectrum; a similar color coding is represented for λ_1. A prominent visual correlation can be seen in FIGURE 10 in that the regions within a part with larger T_e and t_c result in increased λ_1. This result indicates that a larger cooling time (t_c) and end-of-cycle temperature (T_e) are correlated with an increased λ_1.

The machine learning procedures described in Sec. 2.4 were applied to the foregoing data to predict λ_1. The results from a 10-fold training and testing procedure are reported in TABLE 2 presents the performance for the predictive models for all PDAS prediction tasks. The F-score using the Gaussian SVM model is 91% and 71%, respectively, for the 2-way and 3-way classification. The prediction error of λ_1 using the Gaussian SVM regression is ~ 71 nm. Indeed, the linear regression analysis provides similar F-score and RMSE values due to the linear relationship between model features and resulting primary dendritic arm spacing.

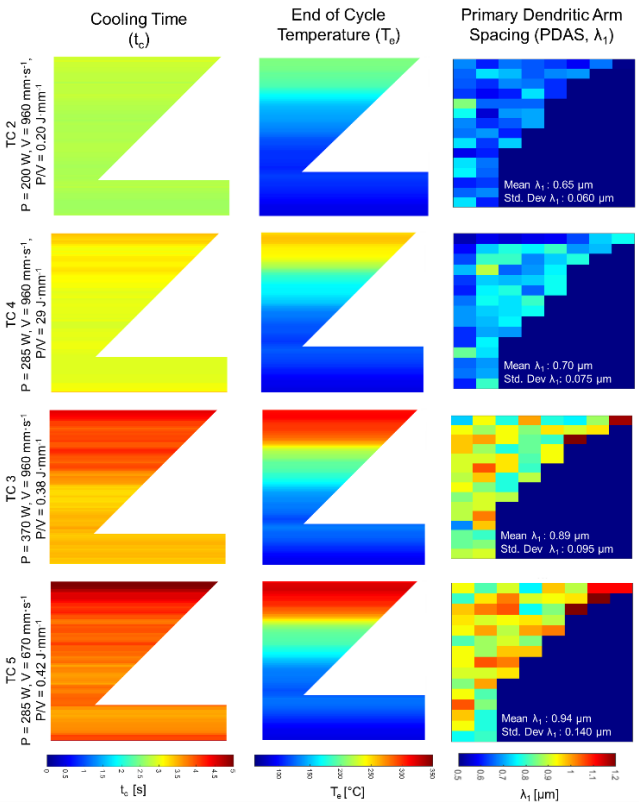

FIGURE 10: PICTORIAL REPRESENTATION OF END-OF-CYCLE TEMPERATURE AND COOLING TIME DERIVED FROM THE GRAPH THEORY THERMAL MODEL AND MEASURED PDAS. AS COOLING TIME AND END-OF-CYCLE TEMPERATURE INCREASES, PDAS INCREASES.

TABLE 2: MACHINE LEARNING RESULTS FOR PDAS PREDICTION FOR SVM AND LINEAR MODELS

Classification F-score (Std.dev)	Task 2A 3-way PDAS (λ_1) classification	Logistic Regression: 70% (8%) **Gaussian SVM: 71% (10%)**
	Task 2B 2-way PDAS (λ_1) classification	Logistic Regression: 88% (11%) **Gaussian SVM: 91% (9%)**
Regression (RMSE)	Task 2C PDAS (λ_1) prediction	Linear Regression: λ_1 = 63 nm **Gaussian SVM Regression λ_1 =71 nm**

3.3 Model Transferability

To alleviate possible overfitting concern resulting from the relatively small data set of PDAS measurements, the models were applied to a separate geometry from a different build plate after training on the data from this work. The experiments underlying these samples are detailed in our prior work, and briefly summarized in the following paragraphs [7].

As shown in FIGURE 11, Two inverted cone geometries were created with Nickel Alloy 718 and were made with two unique parameter conditions, termed fixed and controlled processing. The parts were created on two different build plates created in partnership with Edison Welding Institute on the same open architecture LPBF system used to create the parts in this work. Fixed processing was created with identical nominal process parameters and source powder as this work. Controlled processing conditions changed the laser power to mitigate heat buildup in the sample. The power changes were guided by the graph theory thermal model. The 25mm tall sample cone has an overhang angle of 40°. The laser power for the controlled processed geometry is reduced to 200 W from 285 W at layer 325, and a 10 second dwell time is added after 13 mm of build height. Notably, the model in this work did was not tested with altered laser power and dwell time.

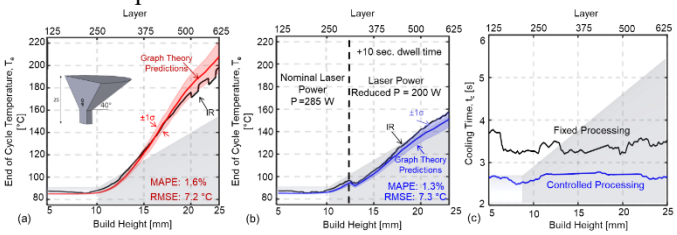

FIGURE 11: (a) END-OF-CYCLE TEMPERATURE FOR FIXED PROCESSED INVERTED CONE. (b) END-OF-CYCLE TEMPERATURE FOR CONTROLLED PROCESSED INVERTED CONE. (c) THE RESULTING COOLING TIME FOR CONTROLLED PROCESSING IS MUCH SMALLER THAT THAT OF FIXED PROCESSING, WHICH INDICATES A SMALLER PDAS RESPONSE

FIGURE 11(a) and (b) shows the predicted end-of-cycle temperature for the fixed and controlled processing conditions. The IR end-of-cycle temperature observations are overlaid on the graphs to show the model accuracy; the MAPE and RMSE for both cases are within 2% and 8 °C, respectively. The simulation was completed in approximately 4 minutes. FIGURE 11(c) shows the predicted cooling time(tc) for these two samples. The increased dwell time and reduced laser power combined to reduce expected cooling time, which results in an expected λ_1 size.

In this build, PDAS (λ_1) measurements were obtained at 6 locations along the build height for each cone part. SEM images are shown in FIGURE 12 along the build height for the fixed and controlled processed cones. The corresponding PDAS (λ_1) measurements are also included. Owing to heat buildup and increased cooling time, the PDAS of the fixed processed cone is $\lambda_1 \approx 700$ nm. In the case of the controlled processed cone, the PDAS is significantly lower ($\lambda_1 \approx 500$ nm) where the laser power change was initiated..

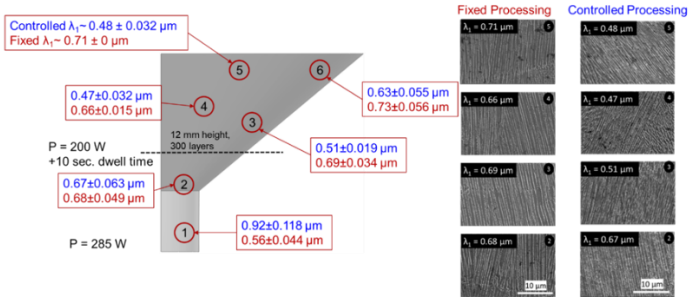

FIGURE 12: PDAS MEASUREMENTS FROM THE INVERTED CONE CASE STUDY ALONG WITH REPRESENTATIVE IMAGES FROM FOUR SELECTED MEASUREMENT REGIONS

Results from the application of the trained model from the parts of this work to the case study work are reported in TABLE 3. Machine learning parameters were not changed, and no data from the cone parts discussed here was used to train the machine learning models used in testing.

The 3-way and 2-way classification results with the Gaussian SVM are 83% and 93%, respectively, while the λ_1 prediction error (RMSE) is approximately 110 nm. These prediction results follow the PDAS prediction results from the previous parts. These results indicate the Task 2 models are capable of transferring to different parts and processing conditions for the Nickel Alloy 718 material system.

TABLE 3: MACHINE LEARNING RESULTS FOR CONE-SHAPED PARTS

Classification F-score (Std.dev)	Task 2A 3-way PDAS (λ_1) classification	Logistic Regression: 71% (9%) Gaussian SVM: 83% (8%)
	Task 2B 2-way PDAS (λ_1) classification	Logistic Regression: 91% (8%) Gaussian SVM 93% (9%)
Regression (RMSE)	Task 2C PDAS (λ_1) prediction	Linear Regression: λ_1 = 80 nm Gaussian SVM Regression λ_1 =110 nm

4. CONCLUSION

We developed and applied a physics and data-integrated approach to predict two critical microstructure characteristics in Nickel Alloy 718 LPBF processed parts, namely the meltpool depth and primary dendritic arm spacing (PDAS, λ_1). A rapid part-scale graph theory thermal model was used to estimate the sub-surface end-of-cycle temperature and cooling time (rate). These simulation-based thermal history features served as inputs to simple machine learning models trained on experimentally acquired data to predict the meltpool depth and PDAS. The approach was demonstrated on Nickel Alloy 718 parts of multiple shapes built under several processing parameter sets with prediction accuracy greater than 80%. In our future research we will expand this prediction approach to more microstructure features, such as grain orientation and microhardness, among others.

ACKNOWLEDGEMENTS

This work was supported by the National Science Foundation (NSF) for funding his work under awards CMMI-2309483/1752069, OIA-1929172, PFI-TT 2322322/2044710, CMMI-1920245, ECCS-2020246, CMMI-1739696, and CMMI-1719388.

All builds and data collection efforts were executed at EWI, and Ajay Krishnan's efforts were sponsored by the EWI Additive Manufacturing.

REFERENCES

[1] Najmon, J. C., Raeisi, S., and Tovar, A., 2019, "2 - Review of additive manufacturing technologies and applications in the aerospace industry," Additive Manufacturing for the Aerospace Industry, F. Froes, and R. Boyer, eds., Elsevier, pp. 7-31.

[2] Blakey-Milner, B., Gradl, P., Snedden, G., Brooks, M., Pitot, J., Lopez, E., Leary, M., Berto, F., and du Plessis, A., 2021, "Metal additive manufacturing in aerospace: A review," Materials & Design, 209, p. 110008.

[3] Mostafaei, A., Zhao, C., He, Y., Reza Ghiaasiaan, S., Shi, B., Shao, S., Shamsaei, N., Wu, Z., Kouraytem, N., Sun, T., Pauza, J., Gordon, J. V., Webler, B., Parab, N. D., Asherloo, M., Guo, Q., Chen, L., and Rollett, A. D., 2022, "Defects and anomalies in powder bed fusion metal additive manufacturing," Current Opinion in Solid State and Materials Science, 26(2), p. 100974.

[4] Snow, Z., Nassar, A. R., and Reutzel, E. W., 2020, "Invited Review Article: Review of the formation and impact of flaws in powder bed fusion additive manufacturing," Additive Manufacturing, 36, p. 101457.

[5] Narasimharaju, S. R., Zeng, W., See, T. L., Zhu, Z., Scott, P., Jiang, X., and Lou, S., 2022, "A comprehensive review on laser powder bed fusion of steels: Processing, microstructure, defects and control methods, mechanical properties, current challenges and future trends," Journal of Manufacturing Processes, 75, pp. 375-414.

[6] Zhao, L., Song, L., Santos Macías, J. G., Zhu, Y., Huang, M., Simar, A., and Li, Z., 2022, "Review on the correlation between microstructure and mechanical performance for laser powder bed fusion AlSi10Mg," Additive Manufacturing, 56, p. 102914.

[7] Riensche, A., Bevans, B. D., Smoqi, Z., Yavari, R., Krishnan, A., Gilligan, J., Piercy, N., Cole, K., and Rao, P., 2022, "Feedforward control of thermal history in laser powder bed fusion: Toward physics-based optimization of processing parameters," Materials & Design, 224, p. 111351.

[8] Yavari, R., Smoqi, Z., Riensche, A., Bevans, B., Kobir, H., Mendoza, H., Song, H., Cole, K., and Rao, P., 2021, "Part-scale thermal simulation of laser powder bed fusion using graph theory: Effect of thermal history on porosity, microstructure evolution, and recoater crash," Materials & Design, 204, p. 109685.

[9] Sanchez, S., Smith, P., Xu, Z., Gaspard, G., Hyde, C. J., Wits, W. W., Ashcroft, I. A., Chen, H., and Clare, A. T., 2021, "Powder Bed Fusion of nickel-based superalloys: A review," International Journal of Machine Tools and Manufacture, 165, p. 103729.

[10] Mostafaei, A., Ghiaasiaan, R., Ho, I. T., Strayer, S., Chang, K.-C., Shamsaei, N., Shao, S., Paul, S., Yeh, A.-C., Tin, S., and To, A. C., 2023, "Additive manufacturing of nickel-based superalloys: A state-of-the-art review on process-structure-defect-property relationship," Progress in Materials Science, 136, p. 101108.

[11] Russell, R., 2019, "NASA's Plans for Development of a Standard for Additively Manufactured Components," Journal of Materials Engineering and Performance, 28(4), pp. 1924-1928.

[12] NASA, 2017, "MSFC-SPEC-3717: Specification for Control and Qualification of Laser Powder Bed Fusion Metallurgical Processes."

[13] Zhang, H., Li, C., Guo, Q., Ma, Z., Li, H., and Liu, Y., 2019, "Improving creep resistance of nickel-based superalloy Inconel 718 by tailoring gamma double prime variants," Scripta Materialia, 164, pp. 66-70.

[14] Watring, D. S., Benzing, J. T., Hrabe, N., and Spear, A. D., 2020, "Effects of laser-energy density and build orientation on the structure–property relationships in as-built Inconel 718 manufactured by laser powder bed fusion," Additive Manufacturing, 36, p. 101425.

[15] Oliveira, J. P., Santos, T. G., and Miranda, R. M., 2020, "Revisiting fundamental welding concepts to improve additive manufacturing: From theory to practice," Progress in Materials Science, 107, p. 100590.

[16] Gouge, M., and Michaleris, P., 2018, Thermo-Mechanical Modeling of Additive Manufacturing, Elsevier, Cambridge, MA.

[17] Luo, Z., and Zhao, Y., 2018, "A survey of finite element analysis of temperature and thermal stress fields in powder bed fusion Additive Manufacturing," Additive Manufacturing, 21, pp. 318-332.

[18] Cole, K. D., Riensche, A., and Rao, P. K., 2022, "Discrete Green's functions and spectral graph theory for computationally efficient thermal modeling," International Journal of Heat and Mass Transfer, 183, p. 122112.

[19] Yavari, M. R., Cole, K. D., and Rao, P., 2019, "Thermal Modeling in Metal Additive Manufacturing Using Graph Theory," Journal of Manufacturing Science and Engineering, 141(7).

[20] Ye, J., Khairallah, S. A., Rubenchik, A. M., Crumb, M. F., Guss, G., Belak, J., and Matthews, M. J., 2019, "Energy Coupling Mechanisms and Scaling Behavior Associated with Laser Powder Bed Fusion Additive Manufacturing," Advanced Engineering Materials, 21(7), p. 1900185.

[21] Reza Yavari, M., Williams, R. J., Cole, K. D., Hooper, P. A., and Rao, P., 2020, "Thermal Modeling in Metal Additive Manufacturing Using Graph Theory: Experimental Validation With Laser Powder Bed Fusion Using In Situ Infrared Thermography Data," Journal of Manufacturing Science and Engineering, 142(12).

[22] Bevans, B., Barrett, C., Spears, T., Gaikwad, A., Riensche, A., Smoqi, Z., Halliday, H., and Rao, P., 2023, "Heterogeneous sensor data fusion for multiscale, shape agnostic flaw detection in laser powder bed fusion additive manufacturing," Virtual and Physical Prototyping, 18(1).

[23] Gaikwad, A., Williams, R. J., de Winton, H., Bevans, B. D., Smoqi, Z., Rao, P., and Hooper, P. A., 2022, "Multi phenomena melt pool sensor data fusion for enhanced process monitoring of laser powder bed fusion additive manufacturing," Materials & Design, 221, p. 110919.
[24] Smoqi, Z., Gaikwad, A., Bevans, B., Kobir, M. H., Craig, J., Abul-Haj, A., Peralta, A., and Rao, P., 2022, "Monitoring and prediction of porosity in laser powder bed fusion using physics-informed meltpool signatures and machine learning," Journal of Materials Processing Technology, 304, p. 117550.
[25] Keshavarzkermani, A., Marzbanrad, E., Esmaeilizadeh, R., Mahmoodkhani, Y., Ali, U., Enrique, P. D., Zhou, N. Y., Bonakdar, A., and Toyserkani, E., 2019, "An investigation into the effect of process parameters on melt pool geometry, cell spacing, and grain refinement during laser powder bed fusion," Optics & Laser Technology, 116, pp. 83-91.
[26] Scime, L., and Beuth, J., 2019, "Melt pool geometry and morphology variability for the Inconel 718 alloy in a laser powder bed fusion additive manufacturing process," Additive Manufacturing, 29, p. 100830.
[27] Vecchiato, F. L., de Winton, H., Hooper, P. A., and Wenman, M. R., 2020, "Melt pool microstructure and morphology from single exposures in laser powder bed fusion of 316L stainless steel," Additive Manufacturing, 36, p. 101401.